Template-free Facile Synthesis of α-MnO₂ Nanorods for Lithium Storage Application

Venugopal Nulu, Arunakumari Nulu, Myeong Geun Kim and Keun Yong Sohn[*]

Department of Nanoscience and Engineering, Center for Nano Manufacturing, Inje University, 197 Inje-ro, Gimhae, Gyeongnam-do 50834, Republic of Korea
[*]E-mail: ksohn@inje.ac.kr

Herein, we report the preparation of α-MnO₂ nanorods by a simple chemical approach following post-annealing treatment, without using any organic or inorganic templates or surfactants. The nanorods have a diameter of 15-50 nm and a length up to 1-3 µm. A preliminary investigation on the formation mechanism of the α-MnO₂ nanorods was carried out. As an anode material for lithium ion secondary batteries, they exhibited high reversible capacity, excellent cycling stability, and excellent rate capability. This outstanding electrochemical lithium storage performance is attributed to the nanorod structure and efficient one-dimensional electron transport pathways. This synthetic procedure is straightforward and low-cost, and thus simplifies the mass production of α-MnO₂ nanorods.

1. INTRODUCTION

Of late, one-dimensional (1D) nanostructures such as nanorods, nanotubes, and nanowires, are the most widely investigated functional nanosystems for nanoscience and technology. Owing to their high aspect ratio, high volume/surface area ratio, and large surface area, metal oxide 1D nanostructures have been studied as potential materials for a broad range of applications including energy storage, catalysis, magnetic, sensors, and biological applications [1]. Among the transition metal oxides, MnO_2 has attracted particular attention because of its easy availability, low raw material cost for synthesis, non-toxicity, and abundance (it is the 12th most abundant element in the earth's crust) [2]. MnO_2 with different crystal morphologies such as α, β, γ, and δ-type, has broad applications in gas sensors [3], water treatment [4, 5], catalysts [6], molecular/ion sieves [7], electrode materials in batteries, and electrochemical capacitors [8-11]. Until now, a variety of MnO_2 1D nanostructures such as nanorods,

nanowires, nanotubes, and nanofibers have been prepared by various synthesis methods: for example, oxidation of Mn^{2+}, reduction of $KMnO_4$, sol-gel pyrolysis, and hydrothermal and refluxing processes [12-21]. However, most of these preparation methods exhibit drawbacks under challenging harsh experimental conditions (high temperature, high pressure, long reaction time, and tedious washing treatment), and require special laboratory glassware and heavy laboratory equipment.

In addition to its abovementioned features, MnO_2 exhibits increased safety margins to overcharge conditions, compared to other transition metal oxides, because of which it has attracted considerable attention as an anode material for Li-ion batteries (LIBs) and in particular for electric vehicles (EVs), which would require substantial quantities of materials to meet the demands of an emerging market. Ever since MnO_2 was recognized as an anode material for LIBs by Poizot et al. [22], other research groups have significantly contributed toward this research [23, 24]. However, compared to intensive research on other transition metal oxides like Co_3O_4, NiO, Fe_2O_3, and Fe_3O_4 as anodes for LIBs, studies on MnO_2 nanomaterials for LIBs are still scarce, because of the various crystallographic forms of MnO_2 such as α-, β-, γ-, and δ-type. Among them, α- and β-MnO_2 can be used as anode materials for LIBs [25-26], whereas γ-MnO_2 serves as a valuable candidate for anode and cathode materials [27]. Further, the electrochemical performance of MnO_2 crystals is related to their morphological structures and crystallographic forms: for example, α-MnO_2 with nanotube morphology [24], γ-MnO_2 crystals with a hollow interior [28], and other 1D MnO_2 nanomaterials exhibit better electrochemical properties than their bulk counterparts [23]. Therefore, it is of prime importance to develop a synthesis method for MnO_2 nanostructures in one crystallographic form, such that it can be executed using simple laboratory equipment, easy experimental steps, and provide yield in gram scale.

In this work, we employed a simple template-free efficient soft chemical approach followed by thermal annealing to fabricate one-dimensional α-MnO_2 nanorods with uniform thickness. This method requires neither a long time nor any complicated process or surfactant. For LIB application, these α-MnO_2 nanorods show good cyclic stability and exceptional rate capability.

2. EXPERIMENTAL

2.1 Material Synthesis

α-MnO_2 nanorods were prepared as follows: In a typical procedure, 5 mmol $KMnO_4$ (Sigma-Aldrich) was dissolved in 100 mL of isopropanol (IPA, Sigma Aldrich) to prepare a transparent and homogeneous solution under constant stirring; a brown precipitate formed immediately. The solution was heated to 60 °C for 2 h, with mild stirring. Within 1–2 h, the color of the solution turned dark-brownish (wine). The obtained precipitate was centrifuged and washed several times with deionized water and ethanol. The formation mechanism of MnO_2 is outlined in equation (1). After washing, the product was dried in a vacuum oven at 110 °C and heated further at 500 °C for 6 h in air.

$$3CH_3CHOHCH_3 + 2KMnO_4 \longrightarrow 3CH_3COCH_3 + 2KOH + 2H_2O + 2MnO_2 \qquad (1)$$
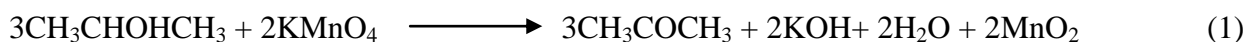
2.2 Characterization

The morphology and microstructures of the α-MnO₂ nanorods were examined by scanning electron microscopy (SEM, JSM7000F, JEOL, Japan), transmission electron microscopy (HR-TEM, JEM-2100F), and energy dispersive X-ray (EDX) spectroscopy. The crystalline structure of the materials was examined by powder X-ray diffraction (XRD) using a Rigaku D/MAX-2200 Ultima diffractometer with Cu-Kα radiation ($\lambda = 1.54056$ Å) in the range $10° < 2\theta < 80°$ operating at 30 kV and 40 mA. N_2 adsorption–desorption isotherms were measured using a Micromeritics ASAP ZOZO instrument at 77 K, and surface areas were calculated by the Brunauer–Emmett–Teller (BET) method.

2.3 Electrochemical measurements

Electrochemical properties of the α-MnO₂ nanorods were measured with CR2032 coin cells. The electrode was prepared by mixing an active material, conductive agent (Ketjen Black), and PAI (polyamide imide) dissolved in N-methyl pyrrolidone (NMP) in the ratio 70:20:10, and coating the slurry on Cu foil. Subsequently, the coated foil was dried in a vacuum oven at 80 °C for 3 h and then at 200 °C for 3 h. The coin-type half-cell was assembled with 1 M $LiPF_6$ EC/DMC 1:1 electrolyte, a Celgard 2300 membrane as the separator, and lithium foil as the counter electrode. Charge/discharge experiments were carried out at different current densities of 50-5000 mA/g with a cut off voltage of 0.01-3.0 V vs. Li^+/Li under ambient condition. Cyclic voltammetry (CV) was performed in the same cutoff voltage range at a scan rate of 0.1 mV/s.

3. RESULTS AND DISCUSSION

The crystallographic phase of the obtained powder was examined by XRD; all diffraction peaks can be readily indexed to the pure tetragonal phase of α-MnO₂ (JCPDS 44-0141), representing the high purity and crystallinity of the final product (as shown in Fig. 1a). Fig. 1b shows the panoramic SEM image of the as-synthesized α-MnO₂ sample. The sample is composed of nanorods with diameters 15-50 nm and length up to 1-3 μm. The inset SEM image in Fig. 1b shows a group of well-grown nanorods (marked with circles), with a diameter of around 50 nm. We believe that during heating, small-width nanorods fuse together to form these specific nanorods; these well-developed thicker nanorods may help withstand the harsh conditions in Li^+ ion electrochemical reactions. An individual group of nanorods together with aggregated nanorod bundles is seen in Fig. 1c, wherein the top inset shows two or three specific α-MnO₂ nanorods of uniform diameter and length, which matches well with the SEM results. The bottom inset is the SAED pattern of the α-MnO₂ sample, which suggests the polycrystalline nature of the nanorods. The HRTEM image of a part of an individual nanorod (Fig. 1d) shows that the nanorod is structurally uniform and crystalline. The lattice spacing of 0.69 nm agrees well with that of the α-MnO₂ (110) plane; the inset shows the partial side TEM view of the thicker nanorod marked with circles as displayed in the above SEM image (Fig. 1b). The elemental composition of the nanorods was estimated by EDX analysis; Fig. 2a shows sharp peaks of Mn, O, and

a little K. The BET specific surface area of our MnO_2 sample is 100.2 m^2 g^{-1} (Fig. 2b); this large specific surface area can be associated with regular and well-distributed nanorods. The isotherms are identified as type IV, which indicates a porous material [23]. The pore size distribution of the sample, calculated from the isotherm using the Barrett–Joyner–Halenda model, is around 12 nm (inset of Fig. 2b).
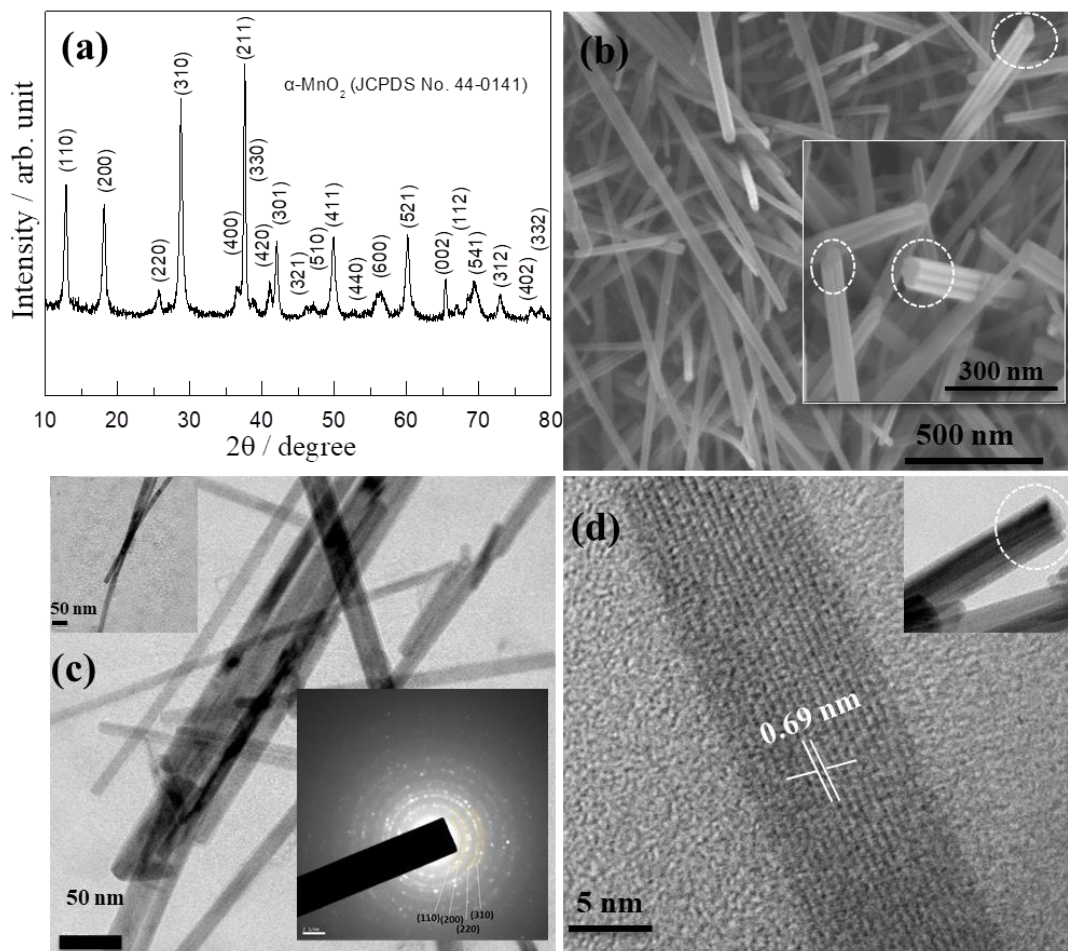

Figure 1. a) XRD pattern, b) SEM image (inset is the magnified FESEM image) and c) TEM image of α-MnO_2 nanorods (insets: top inset is the TEM image of individual nanorods; bottom inset corresponds to the SAED pattern), (d) HRTEM image of the specific nanorod (inset is the TEM image of the well-grown nanorod, clearly marked with circles in the SEM image in Figure 1b).

$KMnO_4$, in neutral conditions under ambient temperature, can oxidize secondary alcohols to their corresponding carbonyl compounds together with MnO_2 and KOH as the significant inorganic byproducts by following the chemical process outlined in equation (1) [29]. During the preparation of MnO_2 nanorods (Scheme 1), firstly, $KMnO_4$ reacts with isopropanol at ambient temperature to produce tiny crystals of MnO_2 generated from Mn^{2+} oxidation in the supersaturation solution, which then grow into colloidal particles.
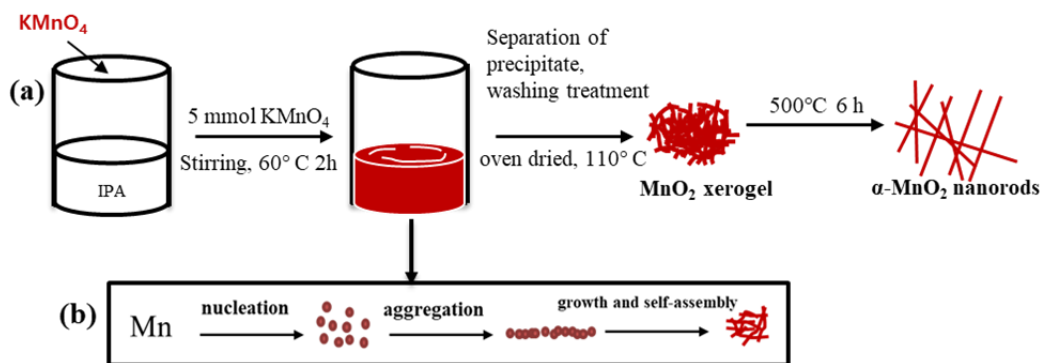
Scheme 1. (a) Schematic representation of the synthesis process of α-MnO$_2$ nanorods, (b) formation procedure for self-assembled MnO$_2$ particles.
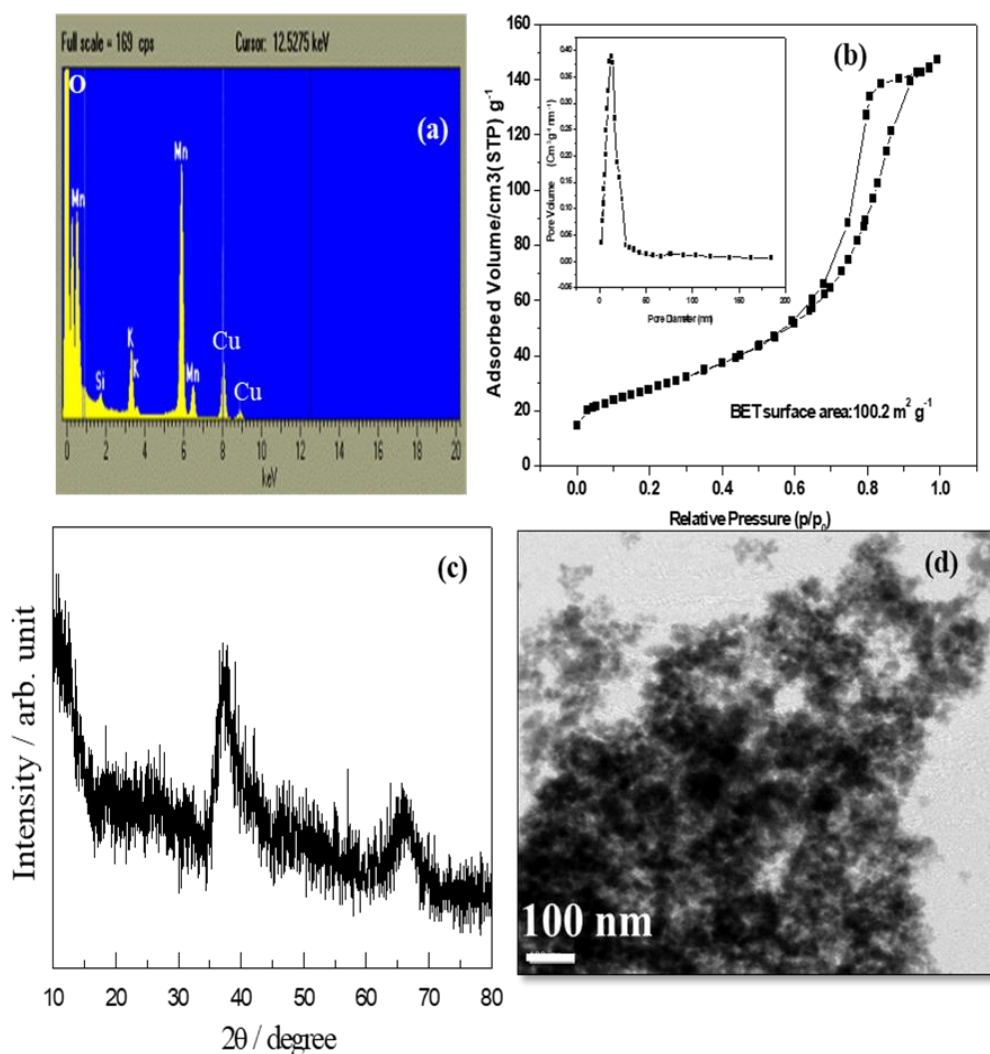

Figure 2. (a) EDX spectrum, (b) N$_2$ adsorption–desorption isotherms for the MnO$_2$ nanorods obtained after calcination (Inset: pore size distribution of nanorods), (c) XRD and (d) TEM images of as-prepared MnO$_2$ xerogel.

   Due to the minimization of interfacial energies, these tiny particles instinctively aggregate into larger continuous porous agglomerates of amorphous MnO_2 (as confirmed by the XRD and TEM images in Fig. 2c and d). The XRD pattern in Fig. 2c is poorly resolved, with two broad peaks at scattering angles of ~37° and ~66°, indicating that MnO_2 was synthesized with a low level of crystallinity. Porous aggregates of low-level crystalline particles are seen in the TEM image of the oven-dried MnO_2 xerogel in Fig. 2d. Heating this sample further at a high temperature in air would preferably encourage the 1D growth of particles, which leads to the formation of nanorods (as shown in Scheme 1). Moreover, calcination removes the moisture and other organic products from the surface that would lead to the formation of defined and well-grown nanorods.
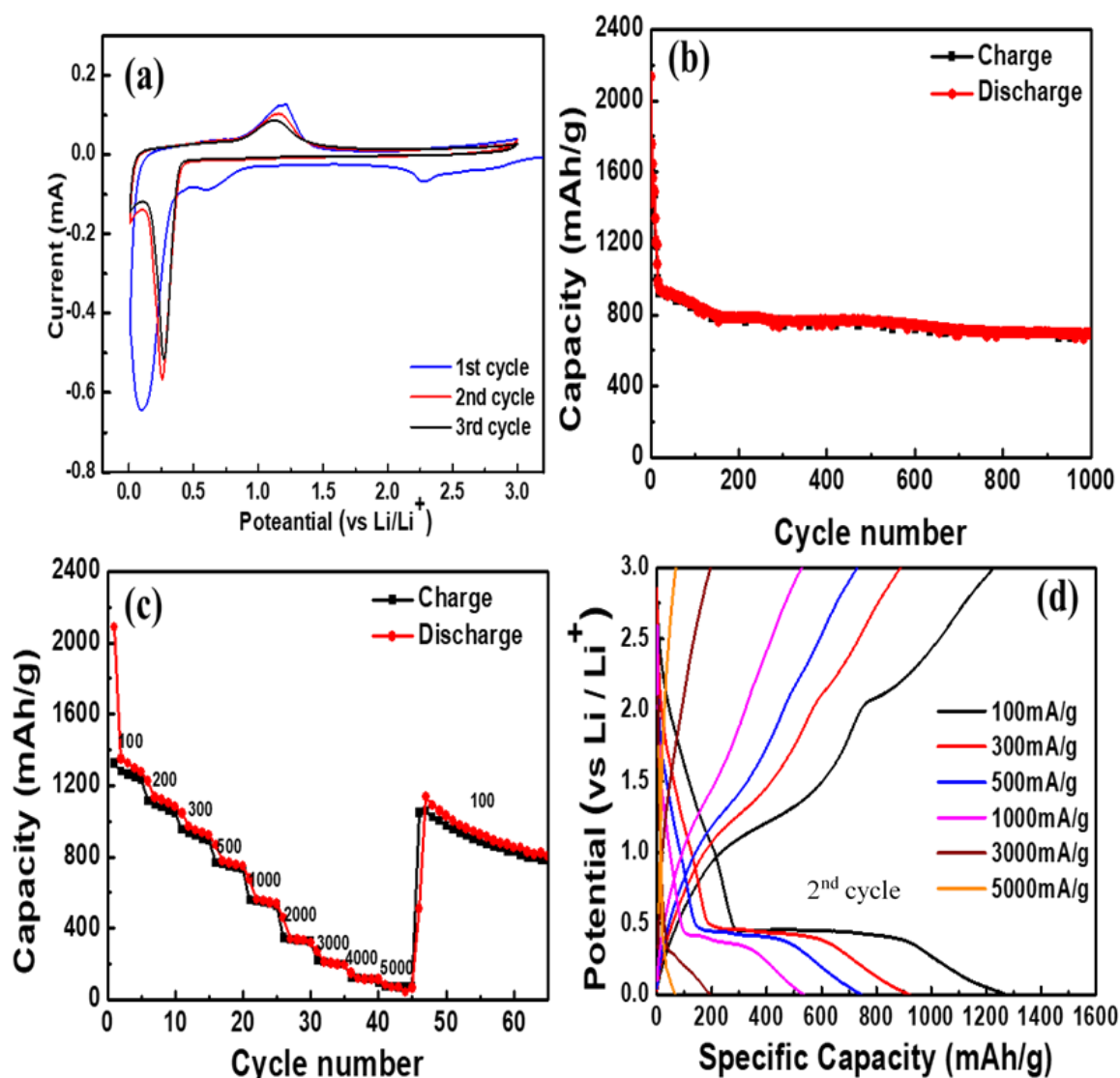

Figure 3. a) CV curves of the MnO_2 nanorod sample at a scan rate of 0.1 mV s^{-1} between 0.05 and 3 V, b) cycling stability of the MnO_2 nanorod electrode tested within the voltage range of 0.01–3 V at 100 mAh g^{-1}, c) Rate capability of MnO_2 nanorod electrode analyzed at room temperature at different current densities, and d) their respective cycling profiles.

When employed as an anode for LIB, initially, CV curves were verified to envisage the electrochemical redox reactions of the MnO_2 nanorod electrode vs. Li^+, as shown in Fig. 3a. The CV plot shows that the reduction peaks of the first, second, and third cycles are approximately at 0.15, 0.3, and 0.3 V, respectively. The first and second CV curves show a marginal shift in the voltage of the reduction peak from 0.15 V to 0.3 V, possibly due to the formation of a solid electrolyte interface (SEI) film. In addition, the peak is stabilized at 0.3 V from the second cycle, which is a typical reduction peak noticed for MnO_2 electrodes [31], which corresponds to the reduction of MnO_2 to Mn^{2+} and the oxidation of Li^+ to Li_2O by the following chemical process.

$$MnO_2 + 4Li+ + 4e^- \rightarrow 2Li_2O + Mn \qquad (2)$$
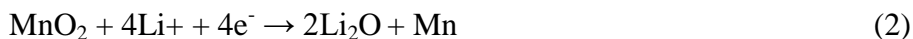
The CV plot of the charging process shows two visible peaks at ~1.3 V, which correspond to Mn/MnO and MnO/Mn_3O_4 redox couples.

$$2Li_2O + Mn \rightarrow MnO_2 + 4Li \qquad (3)$$

The current intensity of the oxidation peak is much lower than that of the reduction peak related to the incomplete conversion of Mn^{2+} to MnO_2 during charging, and the asymmetry CV curves in Fig. 3 reveal that the discharging/charging process is irreversible. However, the CV curves for the second and third cycles are similar in shape, indicating the good reversibility of the electrochemical reactions. Fig. 3b illustrates the cycle performance of the α-MnO_2 nanorods at a current density of 100 mA g^{-1} applied within the voltage range of 0.01–3 V (vs. Li/Li^+) for 1000 cycles. The α-MnO_2 nanorods have a high initial discharge specific capacity of about 2145 mAh g^{-1}, whereas the theoretical discharge specific capacity is 1232 mAh g^{-1}. This significantly extra specific capacity of the MnO_2 nanorod electrode is attributed to the presence of organic and inorganic compounds (LiF, Li_2CO_3, and $ROCO_2Li$) during gel-like SEI film formation on the fresh electrode [31]. Depletion in specific capacity is observed for the initial 15 cycles, following which the specific capacity stabilizes at 900 mAh g^{-1} with a slight decrease in capacity, and after 140 cycles, it is stabilized at about 800 mAh g^{-1}. Finally, the electrode delivers a stable capacity of 780 mAh g^{-1} after 1000 cycles. The capacity retention after 1000 cycles, related to discharge capacities of the MnO_2 nanorod electrode for the 2nd and 15th cycles, is 54% and 86%, respectively. We attributed the initial specific capacity loss to the incomplete decomposition of the SEI film; typically, it takes some cycles to form a stable SEI film on a nano electrode surface, and is a typical electrode behavior noticed in 3d transition metal oxides [30]. However, our electrode delivered remarkable cycle stability for 1000 cycles with excellent capacity, which is much better than that of reported MnO_2 anode electrodes [31-34]. Fig. 3c shows the rate performance of the MnO_2 nanorods, which are ~1334 mAh g^{-1} at 100 mA g^{-1}, ~973 mAh g^{-1} at 300 mA g^{-1}, 790 mAh g^{-1} at 500 mA g^{-1}, and 566 mAh g^{-1} at 1000 mA g^{-1}. Furthermore, the nanorods deliver ~230 mAh g^{-1} at 3000 mA g^{-1}, illustrating the excellent rate performance of this material. After testing at high current densities, we examined the cell again at a low current density of 100 mAh g^{-1}; it regained its discharge capacity of about ~1140 mAh g^{-1}, which is almost the same as that in the initial stages of cycling at the same current density. Comparing the voltage profiles of the MnO_2 nanorod electrodes at different current densities (Fig. 3d), there are two shoulders near 1.2 V and 2.3 V in the charging process at 100 mA g^{-1}, which correspond to Mn/MnO and MnO/Mn_3O_4 redox potentials; these peaks were absent in the charge profiles measured at higher current densities. All the main plateaus of the discharge profiles were located at around 0.4 V. These observed voltage peaks of the

charge/discharge profiles match well with the CV results discussed using Fig. 3a. Compared to other MnO_2-based anodes [37-40], our MnO_2 nanorod electrode shows excellent rate performances and much better cycling stabilities (Fig. 4). A rough comparison of our electrode material, MnO_2 nanorods, with the recently reported other forms of MnO_2 structures, is summarized in Table 1.
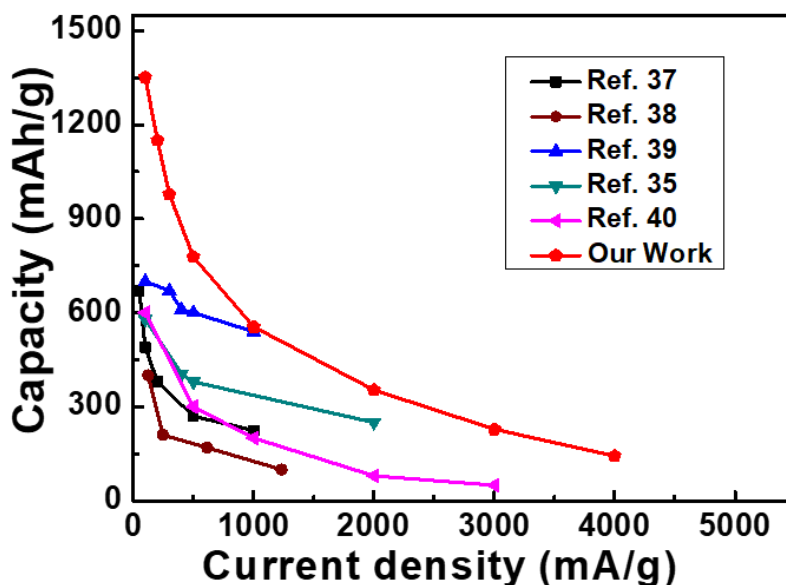

Figure 4. Comparison of the rate performances of our electrode (MnO_2 nanorods) and other reported MnO_2-based anodes for Li-ion batteries.

Table 1. Electrochemical performance comparison of the MnO_2 nanorods reported here with other recently reported MnO_2 structures.

MnO_2 nanostructures	Current density ($mA\ g^{-1}$)	1st discharge capacity ($mAh\ g^{-1}$)	Capacity upon cycling ($mAh\ g^{-1}$)	References
MnO_2	100 mA g^{-1}	2145	860 after 50 cycles	This work
Porous MnO_2 Spheres	200 mA g^{-1}	1750	390 after 50 cycles	41
MnO_2 nanorods and MnO_2 nanorods/ 3D reduced graphene oxide	100 mA g^{-1}	1510 and 1526	220 and 710 after 50 cycles	42
MnO_2@PPy core-shell micromaterials	100 mA g^{-1}	1520	450 after 200 cycles	43
Nanosheet-based MnO_2 hollow capsules	50 mA g^{-1}	1310	210 after 500 cycles	44

The above results confirm that MnO_2 1D nanorods are individually connected as a hierarchical framework with a large surface area and porous surface characteristic. This class of structure can offer a large electrode/electrolyte contact area, which facilitates the passage of lithium ions and electron

transfer through the one-dimensional pathway to the maximum extent, thereby benefitting the rate performance. Moreover, the interconnected nanorod arrangement provides good stability to the electrode against high current densities and maintains the overall structure of the nanorods for a long cycle life.

4. CONCLUSION

In summary, we successfully synthesized hierarchical 1D α-MnO$_2$ nanorods via a simple chemical process for use as the anode material in LIBs. Electrochemical measurements revealed that the given nanorods possess an enhanced specific capacity and augmented cycling stability as an anode material, compared to other reported nanostructured MnO$_2$ electrodes. The superior lithium storage performance was attributed to the structural features of the MnO$_2$ hierarchical 1D framework and the intimate contact between the nanorods, which facilitated maximum lithium ion migration, charge-transport, and electrode stability. The high specific surface area and pore structure of the high-quality well-developed nanorods serve as a buffer for the volume expansion of MnO$_2$ during repetitive conversion reactions, leading to excellent cyclability and superior rate capability. Therefore, these well-grown MnO$_2$ nanorods are highly promising for use as high-performance anodes in LIBs and other energy storage devices like sodium-ion and lithium–air batteries. Moreover, the present synthesis method is simple and effective, and can be easily extended to other materials.

AUTHOR CONTRIBUTIONS
Keun Yong Sohn and Venugopal Nulu drafted the manuscript. Venugopal Nulu designed the experiments, prepared all the samples, and characterized them. Arunakumari Nulu and Myeong Geun Kim performed electrochemical measurements and analyzed the results.

CONFLICTS OF INTEREST
The authors declare no conflict of interest.

References

1. T. Y. Zhai, J. N. Yao, One-Dimensional Nanostructures: Principles and Applications, John Wiley & Sons, Inc., Hoboken, USA, (2013).
2. C.S. Johnson, *J Power Sources*, 165 (2007) 559.
3. W. Zhang, C. Zeng, M. Kong, Y. Pan, Z. Yang, *Sens. Actuator B,* 162 (2012) 292.
4. J. Fei, Y. Cu, X. Yan, W. Qi, Y. Yang, K. Wang, Q. He, J. Li, *Adv Mater.*, 20 (2008) 452.
5. J. Cao, Q. Mao, L. Shi, Y. Qian, *J Mater Chem.*, 21 (2011) 16215.
6. Y.S. Ding, X.F. Shen, S. Sithambaram, S. Gomez, R. Kumar, V.M.B. Crisostomo, S.L. Suib, M. Aindow, *Chem. Mater.*, 17 (2005) 5382.
7. Y. Tanaka, M. Tsuji, Y. Tamaura, *Phys. Chem. Chem. Phys.*, 2 (2000) 1473.
8. Y.S. Horn, S.A. Hackney, C.S. Johnsom, M.M. Thackeray, *J. Electrochem. Soc.*, 145 (1998) 582
9. R.N. Reddy, R.G. Reddy, 2004 *J. Power Sources*,132 (2004) 315.
10. M. Toupin, T. Brousse, D. B´elanger, *Chem. Mater.*, 16 (2004) 3184.
11. V. Subramanian, H. Zhu, R. Vajtai, P.M. Ajayan, B. Wei, *J. Phys. Chem.* B, 109 (2005) 20207.
12. X. Wang, Y.D. Li, *Chem. Commun.*, 124 (2002) 764.

13. R. Yang, Z. Wang, L. Dai, L. Chen, *Mater. Chem. Phys*., 93 (2005) 149.
14. D. Zheng, S. Sun, W. Fan, H. Yu, C. Fan, G. Cao, Z. Yin, X. Song, *J. Phys. Chem.* B, 109 (2005) 16439.
15. Y. Xiong, Y. Xie, Z. Li, C. Wu, *Chem. Eur. J*., 9 (2003) 1645.
16. F. Cheng, J. Chen, X. Gou, P. Shen, *Adv. Mater*., 17 (2005) 2753.
17. E. Machefaux, A. Verbaere, D. Guyomard, *J. Phys. Chem. Solids,* 67 (2006) 1315.
18. F.A. Al-Sagheer, M.I. Zaki, 2000 *Colloids Surf.* A, 173 (2000) 193.
19. Z. Yuan, Z. Zhang, G. Du, T. Ren, B. Su, *Chem. Phys.Lett*., 378 (2003) 349.
20. M. Wei, Y. Konishi, H. Zhou, H. Sugihara, H. Arakawa, *Nanotechnology*, 16 (2005) 245.
21. X. Duan, J. Yang, H. Gao, J. Ma, L. Jiao, W. Zheng, *Cryst Eng Comm*., 2012, 14 (2012) 4196.
22. P. Poizot, S. Laruelle, S. Grugeon, L. Dupont, J.M. Tarascon, *Nature*, 407(2000) 496.
23. F. Cheng, J. Zhao, W. Song, C. Li, H. Ma, J. Chen, P. Shen, *Inorg Chem*., 2006, 45 (2006) 2038.
24. J. Zhao, Z. Tao, J. Liang, J. Chen, *Cryst Growth Des*., 2008, 8 (2008) 2799.
25. J.Cao, Q.H. Mao, L.Shi, Y. T. Qian, *J. Mater. Chem*., 21 (2011) 16210.
26. D.W. Su, H.J. Ahn, G. X.Wang, *J. Mater. Chem. A*, 1 (2013) 4845.
27. J. H. Zeng, Y. F. Wang, Y. Yang and J. Zhang, J. Mater. Chem., 2010, 20, 10915–10918.
28. L. Li, C. Nan, J. Lu, Q. Peng, Y. Li, *Chem. Commun*., 2012, 48 (2012) 6945.
29. L.E. William, B.S. Lily, *J. Am. Chem. Soc*.,44 (10) (1922) 2271.
30. S.W. Lee, C.W. Lee, S.B. Yoon,M.S. Kim, J.H. Jeong, K.W. Nam, K.C. Roh, K.B. Kim, *J. Power Sources*, 312 (2016) 207.
31. Z. Yanhong, C. Gang1, W. Da, S. Chunlai, X. Liping, C. Liang , W. Rui, Z. Nailiang., *Int. J. Electrochem. Sci*., 11 (2016) 2525.
32. L. Hongdong, H. Zhongli, S. Yongyao, H. Rong, T. Liangliang, Z. Lei, R. Haibo, *Int. J. Electrochem. Sci*., 11(2016)8964.
33. H.D. Liu, J. Chen, R. Hu, X. Yang, H.B. Ruan, Y.Y. Su, W. Xiao, J. *Mater. Sci. - Mater. Electron*., 27 (2016) 3968.
34. A. L. M. Reddy, M. M. Shaijumon, S. R.Gowda, P. M.Ajayan, *Nano Lett*., 9 (2009) 1002.
35. A. P. Yu, H. W. Park, A. Davies, D. C. Higgins, A. W. Chen, X. C. Xiao, *J. Phys. Chem. Lett*., 2 (2011) 1855.
36. Y. Y. Li, Q.W. Zhang, J. L. Zhu, X. L. Wei, P. K. Shen, *J. Mater. Chem. A*., 2 (2014) 3163.
37. Y. Jie, G. Xin, C. Liang, W. Nana, J. Xiaolei, X. Huayun, Y. Jian, Q. Yitai, *J. Mater. Chem. A.*, 2 (2014) 17421.
38. J.K. Sue, J.Y. Young, W.K. Ki, C. Changju, J. Sunho, K. Yongku, Y.C. Si, S.L. Sun, C. Sungho, *Chem Sus Chem*., 8 (2015)1484.
39. G. Xianwei, H. Jiuhui, Z. Ling, L. Pan, H. Akihiko, C. Luyang, F. Takeshi, C. Mingwei, *Nanoscale*, 7 (2015) 15111.
40. W.L. Suk, W.L. Chang, B.Y. Seung, S.K. Myeong, H.J. Jun, W.N. Kyung, C.R. Kwang, B.K. Kwang, *J Power Sources*, 312 (2016) 207.
41. Y. Su, J. Zhang, K. Liu, Z. Huang, X. Ren and C.-A. Wang, *RSC Adv.*, 7 (2017) 46263.
42. H. Liua, Z. Hua, Y. Sua, H. Ruana, R. Hua and L. Zhangb, *Appl. Surf. Sci.*, 392 (2017) 777.
43. L. Feng, Y. Zhang, R. Wang, Y. Zhang, W. Bai, S. Ji, Z. Xuan, J. Yang, Z. Zheng and H. Guan, *Nanoscale Res. Lett.*, 21 (2017) 518.
44. Y. Wang, P.-S. Ding, M.-G. Zou, W.-B. Guo, D.-X. Wang and F.-C. Zhang, *Ferroelectr.*, 522 (2018), 75.